

GROWING LIVE DISKS WITHIN COSMOLOGICALLY ASSEMBLING ASYMMETRIC HALOS: WASHING OUT THE HALO PROLATENESS

INGO BERENTZEN AND ISAAC SHLOSMAN

Department of Physics and Astronomy, University of Kentucky, Lexington, KY 40506-0055, USA

email: iberent@pa.uky.edu, shlosman@pa.uky.edu

Submitted to Astrophysical Journal

ABSTRACT

We study the growth of galactic disks in live triaxial dark matter (DM) halos. The halos have been assembled using the constrained realizations method and evolved from the linear regime using cosmological simulations. The ‘seed’ disks have been inserted at redshift $z = 3$ and increased in mass tenfold over various time periods, $\sim 1 - 3$ Gyr, with the halo responding quasi-adiabatically to this process. We follow the dynamical and secular evolution of the disk-halo system and analyze changes in the most important parameters, like three-dimensional DM shapes, stellar (disk) and DM (halo) radial density profiles, stellar bar development, etc. We find that a growing disk is responsible for washing out the halo prolateness and for diluting its flatness over a period of time comparable to the disk growth. Moreover, we find that a disk which contributes more to the overall rotation curve in the system is also more efficient in axisymmetrizing the halo, without accelerating the halo figure rotation. The observational corollary is that the maximal disks probably reside in nearly axisymmetric halos, while disks whose rotation is dominated by the halo at all radii are expected to reside in more prolate halos. The halo shape is sensitive to the final disk mass, but is independent of how the seed disk is introduced into the system — abruptly or quasi-adiabatically. It is weakly sensitive to the timescale of the disk growth. We also expect that the massive disks are subject to a bar instability, while light disks have this instability damped by the halo triaxiality. Implications of these results to the cosmological evolution of disks embedded in asymmetric halos are discussed and so are the corollaries for the observed fraction of stellar bars. Finally, the halo responds to the stellar bar by developing a gravitational wake — a ‘ghost’ bar of its own which is almost in-phase with that in the disk.

Subject headings: galaxies: evolution – galaxies: formation – galaxies: halos – galaxies: kinematics and dynamics – galaxies: structure – cosmology: dark matter

1. INTRODUCTION

A great deal of effort has been invested during the last couple of decades in understanding the large-scale structure formation in the Universe. While a substantial progress has been made in following the hierarchical buildup of dark matter (DM) halos, the structure development on subgalactic scales, such as the growth of disks, bulges, central black holes, etc., is only now being investigated. In this paper we study the buildup of stellar disks immersed in evolving DM halos of an arbitrary shape obtained in cosmological simulations and the concurrent symbiotic evolution of the disk-halo system. Specifically, we analyze the change in the halo triaxiality to the growing disk and its feedback onto the disk evolution.

Beyond the active and passive adjustments of the halo to the growing disk and *vice versa*, the disk is prone to a number of dynamical instabilities, such as the bar instability, which can alter the evolution of the system in the most profound way. A strong and massive stellar bar will facilitate the angular momentum and mass redistribution within the disk and between the disk and the halo (e.g., Athanassoula 2003). The efficiency of this process is not yet fully understood but is known to depend on a number of parameters such as the dispersion velocities in the halo, its mass concentration, etc.

First, from the most general dynamical considerations, the coupled dynamical evolution of a disk-halo system is expected to depend on the prevailing shape of the DM

halo and its embedded disk as well as on the ability of the disk to develop a strong stellar bar. While DM halos form on the average as highly triaxial (i.e., prolate and flat) systems in cosmological numerical simulations (e.g., Bullock 2002 for a review), they appear nearly axisymmetric (i.e., oblate) in the local Universe (e.g., Rix & Zaritsky 1995; Merrifield 2002). What process(es) drive this axisymmetrization of the halo?

Second, the halo radial density profile can have an effect on its coupling to the growing disk, especially on the efficiency of the angular momentum transfer to the halo. It was argued that cuspy halos (i.e., Navarro, Frenk & White 1997, hereafter NFW) provide a substantial drag on the stellar bars (e.g., Weinberg 1985; but see Sellwood 2006) and the feedback is capable of leveling off the density cusp (Weinberg & Katz 2002; Holley-Bockelmann, Weinberg & Katz 2005), although this latest point is a matter of controversy (Sellwood 2003; McMillan & Dehnen 2005).

Baryons have been shown to modify both the radial density profile and the triaxiality of the DM halo — dumping baryons within the halo dilutes the triaxial potential (Dubinski 1994; Kazantzidis et al. 2004) and clumpy baryons can level off the density cusp (El-Zant, Shlosman & Hoffman 2001). However, the halo triaxiality (at each radius) can also decrease during the violent phases of major mergers as they come from random directions and during the quiescent phases of slow accretion (outside the halo cusp) — this type of halo evolution is

actually implemented in the current work.

The fraction of stellar bars at cosmological distances is of course an interesting parameter which can provide us with clues to the evolution of galaxies over the Hubble time. The original claim that the observed bar fraction decreases sharply over redshifts $z \gtrsim 0.5$ (Abraham et al. 1999) has been questioned first because of the specific method of bar detection used in this work (Jogee et al. 2002a,b). More broadly, analysis of the *HST* GEMS¹ survey of about 1,600 galaxies has shown that the fraction of strong bars in the optical stays unchanged to $z \sim 1$, i.e., lookback time of 8 Gyr (Jogee et al. 2004), which was confirmed for much smaller samples (Sheth et al. 2003; Elmegreen et al. 2004). Moreover, Jogee et al. have concluded that the distributions of bar lengths and their axial ratios is largely preserved as well — with a corollary for disk and DM halo properties. Overall, this means that since $z \sim 1$ at least, the galaxy evolution is probably not driven by major mergers but entered the quiescent phase.

This result can be coupled to a more general issue of the DM halo shape evolution. El-Zant & Shlosman (2002) used the method of Liapunov exponents to calculate the fate of bars in mildly triaxial *rigid* halos. They found that the bars cannot be sustained in these configurations due to the generated chaos. Berentzen, Shlosman & Jogee (2006) have extended this work to include the self-consistent models with live triaxial halos, i.e., flat and prolate.² In all cases, bars which formed as the initial disk response to the halo prolateness have dissolved over \sim Gyr timescale, i.e., few bar rotations. The series of models with increasing cuspiness in the halo have shown that the chaos generated by bars tumbling in triaxial halos can also wash out the halo prolateness and thus the bar may survive. But it remained unclear whether the decrease in the halo triaxiality detected by Berentzen et al. is related to the halo relaxation because of the insertion of a massive axisymmetric disk or it is the result of the response in the disk to the halo asymmetry. Our present work provides a compelling answer to this question.

The disk formation within a DM halo has been studied before under a long list of simplifying assumptions (e.g., Sommer-Larsen et al. 2003; Immeli et al. 2004; Governato et al. 2006). Here we focus on the disk-halo interaction and its effects on the developing disk morphology and the feedback onto the halo shape. To follow the disk-halo evolution in a more realistic environment, we monitor the halo assembly in the cosmological framework starting with a 2.5σ linear perturbation in the expanding universe, using the constrained realizations algorithm (Hoffman & Ribak 1991) to prescribe the initial conditions. We insert a small ‘seed’ stellar disk of about 10% of its final mass within the halo which experiences a quiescent phase of its dynamical evolution. The disk then grows substantially in size and in mass via self-similar mass addition over time periods of $\sim 1 - 3$ Gyr. We analyze the subsequent evolution of such a disk-halo system and provide a comparison with simplified versions of this system. Those include isolated, axisymmetric and triax-

ial halos with non-evolving light and massive disks.

This paper is structured as following: Section 2 deals with the details of numerical modeling. Results are given in Section 3 and discussed in Section 4.

2. NUMERICAL MODELING

We have used the updated version FTM-4.4 of our hybrid code (e.g., Heller & Shlosman 1994; Heller 1995) with the total $N \sim 1.3 \times 10^6$ particles, of which 1.2M represent the collisionless DM and 100K — the collisionless baryonic components, respectively. The gravitational forces have been computed using Dehnen’s (2002) *falcon* force solver, a tree code with mutual cell-cell interactions and complexity $O(N)$. It conserves momentum exactly and is about 10 times faster than optimally coded Barnes & Hut (1986) tree code. The gravitational softening of 200 pc to simulate both the evolution of the DM component and that of the baryons in the disk has been implemented.

We have introduced the following dimensionless model units. The spatial distance unit is taken as $r = 10$ kpc, the mass unit is $M = 10^{11} M_\odot$ and the gravitational constant is chosen to be $G = 1$, which results in a time unit of $\tau = (r^3/G M)^{1/2} = 4.7 \times 10^7$ yrs. The dynamical timescale, τ_{dyn} within 10 kpc is $\sim 4 \times 10^7$ yr for the pure DM halo. In these units, the velocity is given in 208 km s^{-1} . The actual physical units are mostly used here.

2.1. Initial conditions

We have used the constrained realizations technique (Hoffman & Ribak 1991; see Section 2.1.1 below) to construct a DM halo, and followed its assembly in the expanding Friedmann universe. At redshift $z = 3$, we have introduced a live ‘seed’ stellar disk into the halo and grew it over the next $\sim 1 - 3$ Gyr, depending on the model.

Vacuum boundary conditions and physical coordinates have been used ignoring the cosmological constant term and assuming the open CDM (OCDM) model with $\Omega_0 = 0.3$, $h = 0.7$ and $\sigma_8 = 0.9$. Here Ω_0 is the current cosmological density parameter, h is the Hubble constant normalized by $100 \text{ km s}^{-1} \text{ Mpc}^{-1}$, and σ_8 is the variance of the density field convolved with a top-hat window of radius $8h^{-1}$ Mpc used to normalize the power spectrum (see also Romano-Diaz et al. 2006a,b). Because we are interested in the evolution on the sub-galactic scales, the difference with the Λ CDM cosmology is small and our results should also stand for the latter. The FTM-4.4 has been tested in the cosmological context using the Santa Barbara Cluster model (Frenk et al. 1999). Further details are given in Romano-Diaz et al. (2006b).

2.1.1. The Halo: Constrained Realizations

The constrained realizations algorithm (Hoffman & Ribak 1991) was used by applying linear constraints to specify the initial density field in specified locations and evaluated with Gaussian smoothing kernels. The width of a kernel has been fixed and corresponds to the mass scale on which the constraint has been imposed. Within the context of the cosmological model and assuming the power spectrum of the primordial perturbation field, we have generated a constrained realization of the density field from a random realization of this field.

¹ Galaxy Evolution from Morphology and SEDs (Rix et al. 2004)

² i.e., $b > c$ and $a > b$, respectively, where a, b and c are the halo principal axes.

The simulations start at redshift $z = 120$, corresponding to $\tau = 0.0127$ Gyr, and ends at $z = 0.0$. The DM model has been constructed in such a way as to have a set of constraints all located at the origin. The corresponding nested set of perturbations has been designed to collapse off-center. These density constraints constitute $2.5 - 3.5\sigma$ perturbations, where σ^2 is the variance of the smoothed field, which were imposed on 128^3 cubic grid with a side of $4h^{-1}$ Mpc. The total mass of the DM is $\sim 10^{12}h^{-1}M_\odot$ and it is embedded in a region corresponding to a mass of $10^{13}h^{-1}M_\odot$ in which the overdensity is zero of unperturbed Friedmann model. The three nested off-center perturbations of $\delta = 6.0, 4.6$ and 3.4 , corresponding to the mass scale of $9.37 \times 10^{10}h^{-1}M_\odot$, $1.87 \times 10^{11}h^{-1}M_\odot$ and $3.75 \times 10^{11}h^{-1}M_\odot$, are designed to collapse by $z_{\text{coll}} = 5.7, 3.8$ and 2.2 , respectively. Over the time of the simulation, the density field has been sampled with 500–1,000 time outputs.

For the reference, the halo mass within 10 kpc is about 1.5 (or 165K particles), from $\tau = 38$, or $z \approx 3$ (just prior to the seed disk insertion) to the end of the evolution at $z = 0$ ($\tau = 239$). This is about two orders of magnitude above the halo sampling in cosmological simulations.

2.1.2. The seed disk

The initial ‘seed’ disk is a Miyamoto-Nagai (1975) disk described by the gravitational potential:

$$\Phi_D = -\frac{G M_D}{\sqrt{x^2 + y^2 + (A_D + \sqrt{B_D^2 + z^2})^2}}, \quad (1)$$

where the scalelengths A_D and B_D , and the disk mass M_D are given in Table 1. To include the stellar disk in our models, we first determine the main principal axes of the triaxial halo, based on its moments of inertia. We then introduce the disk with its rotation axis being aligned with the halo minor axis. As we show in Section 3.1, the halo figure is nearly stagnant over the Hubble time. The disk is placed with the center of mass position and velocities of the main halo, iteratively measured in spheres with radii going from 50 kpc down to 0.5 kpc. Since the halo is not in equilibrium and the initial disk mass is negligible compared to that of the halo, we do not require the halo to relax on the introduced potential. The disk is inserted at a redshift $z = 3$, well after the last major merger (see Section 3).

2.1.3. Growing a disk within the live halo

To simulate the process of disk formation in a simplified way, the disk is gradually grown from the seed, by adding stellar particles to it, based on the probability given by the Miyamoto-Nagai density distribution. The central volume density of the disk is kept constant during this time period, and we adjust (i.e., increase) the radial and vertical scalelengths of the disk correspondingly, keeping the ratio B_D/A_D constant. Recent analysis of the GEMS galaxies supports such a disk buildup, when the surface density does (nearly) not change with redshift while the disk mass increases with time (Barden et al. 2005).

Since the equatorial plane of the disk may change owing to a (slow) inner halo figure tumbling in 3-D, we determine the instantaneous disk plane from its moments of

TABLE 1
DISK MODEL PARAMETERS

Model	M_D	A_D	B_D	R_{cut}	N_D
D1	0.0612	0.132	0.023	1.16	10 000
	0.6120	0.284	0.050	2.50	100 000
D2	0.1838	0.132	0.023	1.16	10 000
	1.8375	0.284	0.050	2.50	100 000

NOTE. — Columns: (1) the disk model; (2) mass; (3) radial scalelength; (4) vertical scalelength; (5) outer disk cutoff; (6) number of particles. The upper lines in D1 and D2 correspond to initial and final values of disk parameters, at τ_i and τ_f

TABLE 2
SIMULATIONS

RUN	Disk	τ_i [Gyr]	τ_f [Gyr]	Comments
A 0	—	—	—	pure live DM model
A 1	D 1	1.81	2.84	default model
A 1b	D 1	1.81	2.84	as A1, growing frozen disk
A 2	D 1	1.81	2.84	growing thin disk, live halo
A 3	D 1	1.81	2.84	growing disk, frozen halo
A 4	D 1	1.81	4.87	slowly growing disk, live halo
A 5	D 1	—	—	non-growing disk, live halo
A 6	D 1	—	—	low J disk, live halo
B 1	D 2	1.81	2.84	more massive disk, live halo
B 5	D 2	—	—	non-growing massive disk, live halo
C 1	D 1	1.81	2.84	growing disk, live axisymmetric halo
C 6	D 1	—	—	non-growing disk, live axisymmetric halo

NOTE. — Columns: (1) the model; (2) the disk model (see Table 1); (3) the start time of the disk growth; (4) the end time of the disk growth

inertia. Then, based on the radial force component at the position of the new particles, we assign the corresponding circular velocity (without any additional dispersion or z -velocity component (relative to the disk equatorial plane).

This method, strictly speaking, does not grow the disk under exact equilibrium conditions, but we do not expect this in a realistic disk formation either, i.e., most likely it involves some degree of relaxation as well. We impose a linear mass growth over a specified time period, starting with redshift $z = 3$ (see Table 2). Overall, the disk mass grows by a factor of ten over ~ 1 Gyr or ~ 3 Gyr, which corresponds approximately to $\Delta\tau = 22$ and 60 . Because the disk center-of-mass position and the 3-D orientation of the disk depend on the large-scale motions within the surrounding halo and on the streamers on even larger scale in the DM, we have developed a new diagnostics to address the evolution of disk intrinsic parameters, such as the bar pattern speed.

3. RESULTS

3.1. Evolution of the pure DM halo — model A0

We evolve the halo model from $z = 120$ till $z = 0$, or $\tau \approx 0.013$ Gyr and 11.3 Gyr, respectively. We analyze the evolution of a diskless halo in the cosmological background for further comparison with halos that harbor light, massive or growing disk models.

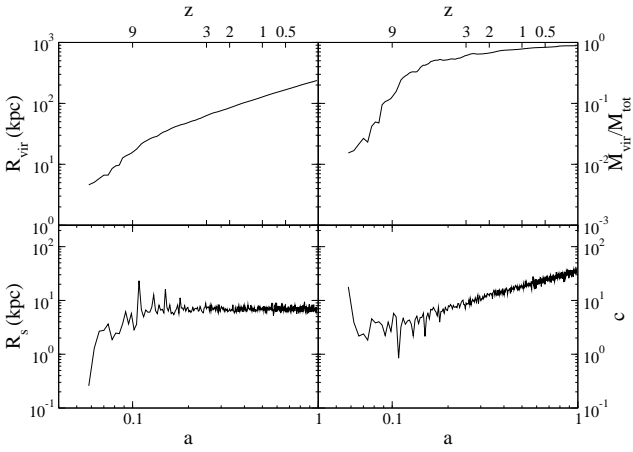


FIG. 1.— Evolution of the NFW scale radius R_s , the virial radius R_{vir} , the concentration parameter $C \equiv R_{vir}/R_s$ and the virial-to-total mass ratio M_{vir}/M_{tot} , as a function of redshift z and cosmological expansion factor a in the pure halo model A0.

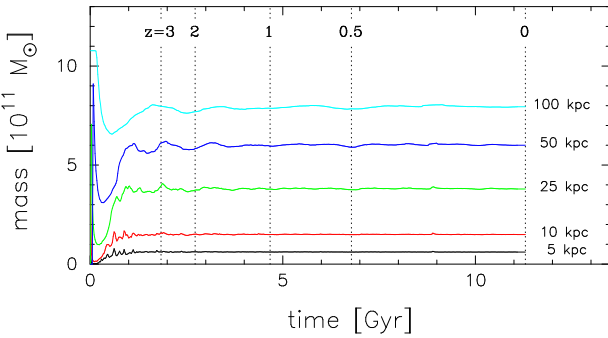


FIG. 2.— Halo mass in the pure halo model A0 within spherical radii and as a function of time. The different lines show the mass evolution within spheres of constant radii, centered on the main halo. The dashed vertical lines mark, from left to right, redshifts $z = 3, 2$ and 1 , respectively.

Initially, the DM expands with the Hubble flow, but detaches and starts its collapse by $z \sim 15$. The epoch of major mergers ends around $z \sim 7$, as given by the evolution of the NFW scale radius R_s and the halo virial radius³ R_{vir} . These parameters experience abrupt increases during each violent event, as shown in Fig. 1

³ We define the virial radius R_{vir} from $M_{vir} = (4\pi/3)\rho R_{vir}^3$, where M_{vir} is the virialized mass and the current mean density $\rho = \Delta_c \rho_{crit}$, with Δ_c being the current virial overdensity and ρ_{crit} — the critical density in the universe at this time.

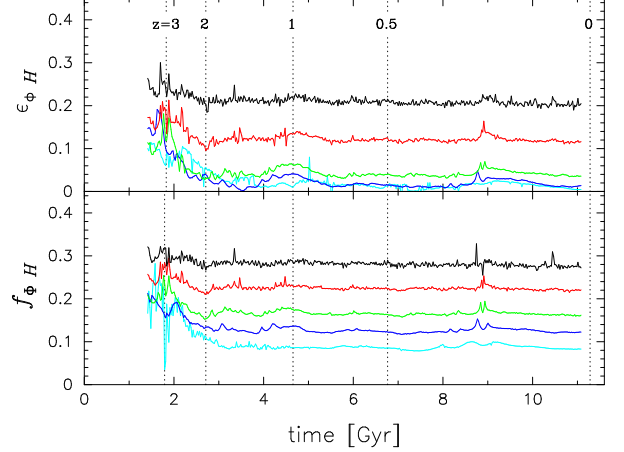


FIG. 3.— Halo shapes based on the *isopotential* contours as a function of time in the model A0. The different colors represent the prolateness, $\epsilon_{\Phi H} \equiv 1 - b/a$ (upper panel), and flatness, $f_{\Phi H} \equiv 1 - c/a$ (lower panel) at different radii (black: 5 kpc, red: 10 kpc, green: 25 kpc, blue: 50 kpc, and cyan: 100 kpc).

(e.g., Romano-Diaz et al. 2006a,b). Following the violent epoch, R_s remains constant at ~ 7 kpc for the rest of the simulations. R_{vir} grows linearly between the mergers and during the quiescent accretion phase which follows. The latter phase includes the minor mergers as well that occur at all redshifts leading to the continuous growth of the virialized-to-total halo mass ratio (Fig. 1). Fig. 2 displays the halo mass growth characterized by the mass assembly within the spherical radii of 5 kpc, 10 kpc, 25 kpc, etc. The overall halo assembly in the cosmological background is shown in the Animation Sequence 1. After $z \sim 3$, the central 50 kpc of the halo contains about 650,000 particles. The virialization proceeds from inside out: while the inner 10 kpc virialize during the first 1 Gyr, the outer 100 kpc virialize after 2–3 Gyr. The NFW density profile is established early, by $z \sim 10$.

The dimensionless cosmological spin parameter for the halo (e.g., Peebles 1969), $\lambda \equiv J|E|^{1/2}/GM^{5/2}$, calculated within R_{vir} decreases with time from ~ 0.1 at $z \sim 9$ to about 0.013 at $z \sim 1$, or stays a constant, $\lambda_s \sim 0.1$ within R_s , using notation of Bullock et al. (2001). Here, E , J and M are the total energy, angular momentum and mass of the halo. These values correspond to the tail of the average λ in numerical simulations (e.g., Barnes & Efstathiou 1987), because we neglect the outer tidal fields which become important at lower redshifts.

For our study of a disk evolution within the live halo, the halo shape, especially its prolateness, is of a prime importance. Fig. 3 shows the halo prolateness $\epsilon_{\Phi H} = 1 - b/a$ and its flatness $f_{\Phi H} = 1 - c/a$ as a function of time, based on a numerically stable ellipse fitting (Halir & Flusser 1998) of the *isopotential* contours, for different radii. We note that the isopotentials have a clear advantage over the isodensity contours, being much less noisy (Berentzen et al. 2006). At the same time the values of ϵ_{Φ} and f_{Φ} reflect the integral properties of the system and have significantly smaller values than those of ϵ_{ρ} and f_{ρ} used in the literature and based on fitting the isodensity contours.

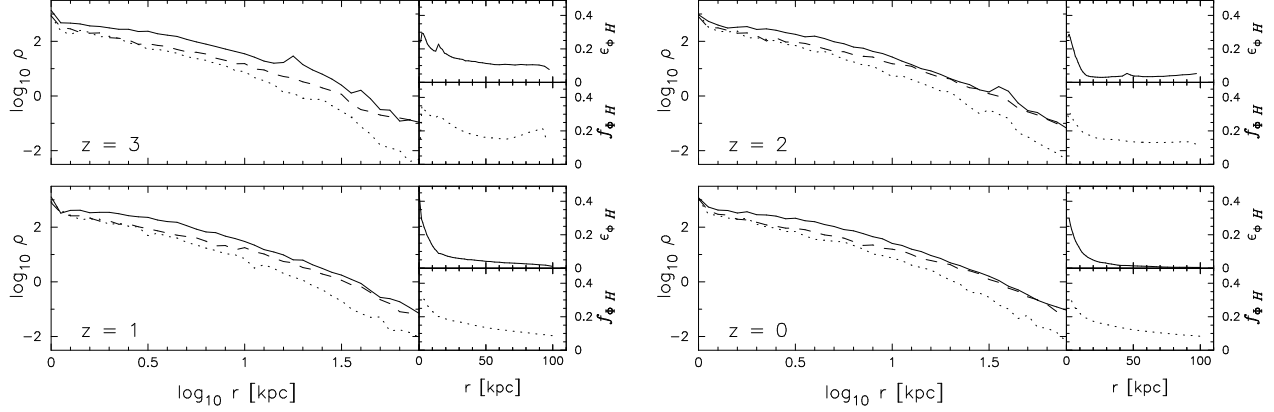


FIG. 4.— Pure DM halo model A0. The figure shows the volume density, in units of $10^6 M_\odot \text{ kpc}^{-3}$, along the halo principal axes (left panel). The right panels show the halo prolateness (upper panel) and its flatness (lower panel). The four frames are taken at different redshifts, $z = 3, 2, 1$ and 0. The overall halo evolution in the cosmological background is shown in the Animation Sequence 1.

After about 3 Gyr the halo shape evolves in a quiescent manner, largely in response to the slow accretion. The halo prolateness and flatness decrease outwards with time because of our neglect of the large-scale tidal field, i.e., absence of periodic boundary conditions. The former becomes small beyond ~ 25 kpc radius, while the latter is significant at all radii. Except for occasional bumps, that reflect the halo substructure (i.e., subhalos), both parameters change little with time. It is important that the inner halo remains prolate and in a quasi-steady state in this pure halo model.

In Fig. 4 we display four snapshots of the halo volume density along its principal axes at different redshifts. These axes have been determined using moments of inertia. We also show the radial profiles of halo prolateness and flatness. At $z = 3$ (or $\tau = 1.81$ Gyr) — the time of the seed disk insertion, the halo is prolate, with $\epsilon_{\Phi H}$ just below 0.3 at the center, decreasing to below ~ 0.1 outside 100 kpc. By $z \sim 2$, the halo prolateness is largely washed out outside the inner 25 kpc, while halo flatness remains significant everywhere. This detail is important for understanding the evolution of disks immersed in the halo, specifically for the bar instability — the outer halo becomes largely axisymmetric in a couple of Gyrs after $z \sim 3$. This happens because of the slow accretion of the DM in the absence of the large-scale tidal torques. However, it is important that the *inner* halo, within the central 20 kpc, remains significantly prolate and hence will interact specifically with the immersed disk.

3.2. Evolution with growing disks

3.2.1. Inserting a disk: the halo relaxation effects

Next, we compare the halo evolution when the disk is immersed in a number of different ways. The first possibility is when a *seed* disk is introduced either abruptly or more adiabatically at $z = 3$. The mass of the seed disk is small, 10% of its final mass and smaller than the halo mass within the disk radius by more than an order of magnitude. The disk grows to its final mass within ~ 1 Gyr, i.e., $\tau \sim 22$ or in a less intrusive way over a longer period of time, ~ 3 Gyr, i.e., $\tau \sim 60$. To verify that an abrupt positioning of the disk within the halo does not produce any visible effects on the halo evolu-

tion, even more adiabatic insertion of the seed disk is performed as follows. The disk is brought up gradually over $\Delta\tau = 10$ or 20, keeping the disk particle positions frozen, but correcting for the disk center-of-mass with respect to the halo. In these test models, the disk reaches its *seed* mass always at $z = 3$ ($\tau = 38$). At this moment we unfreeze the particles and grow the disk tenfold thereafter. We perform a number of tests where the basic halo parameters are compared between the models (see Tables 1 and 2).

We note that the outer part of the halo itself is not in a virial equilibrium, and that the seed disk is dominated completely by the halo mass at all radii. The major parameters we are concerned with are the halo flatness, $f_{\Phi H}$, and especially its prolateness, $\epsilon_{\Phi H}$. We have run a number of test models in order to understand to what degree the subsequent evolution of the halo shape depends upon the method of disk insertion. We started to bring up the frozen seed disk at $\tau = 18$ (~ 0.8 Gyr) over the time of 0.47 Gyr and at $\tau = 28$ (~ 1.3 Gyr) over the time of 0.94 Gyr. So by $z = 3$, the halo feels the full seed disk potential, and the disk starts to grow tenfold. In all cases the model is evolved for more than 4 Gyr thereafter. We find that various tracks, displaying the host halo prolateness and flatness in these test models, are nearly identical up to $z \sim 3$, when the disk evolution takes over and the curves separate. This means that the diverging evolution we observe in some of the models is not the result of the halo response to the disk insertion but of other factors, such as the disk evolution, discussed in the next sections.

Before we discuss in detail the evolution of the key models, we show the halo response to the disk for the few most relevant cases: model A5 (a non-growing disk), model A1 (a standard seed disk growing tenfold), model A4 (same as A1 but a disk growing over 3 Gyr), model B1 (a seed disk growing to a massive disk), and model A1b (identical to A1, but the disk is growing and remaining in the frozen state). Fig. 5 displays $\epsilon_{\Phi H}$ and $f_{\Phi H}$ taken at 5 kpc for these models. The most dramatic decrease in the halo prolateness we observe in B1, where, unlike in B5, the disk grows in mass. This model loses all of its initial prolateness in the inner halo over the first \sim

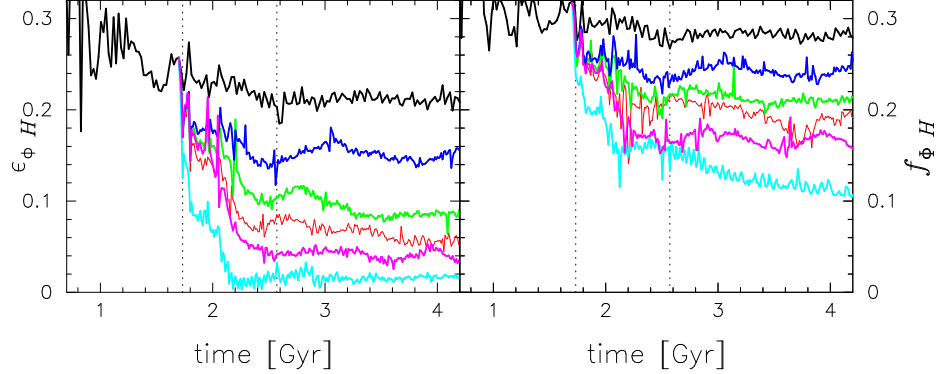


FIG. 5.— Evolution of the halo prolateness (left) and flatness (right) at 5 kpc in different model realizations. The model colors are: pure DM halo A0 (black), our benchmark model with a growing disk A1 (red), slowly growing A4 (green), non-growing A5 (blue), frozen growing disk A1b (magenta), massive growing disk B1 (cyan). Vertical dotted lines are $z = 3$ and 2 (left-to-right).

1 Gyr. The model A1 loses most of its prolateness as well, while A4 mimics its evolution with a somewhat more prolate and flat halo. Interestingly, the model A1b with the frozen growing disk has a small but measurably larger impact on the halo shape than the live A1 disk — to be discussed in Section 4. The model A5 with a non-growing seed disk leads to a much smaller decrease in $\epsilon_{\Phi H}$. The pure DM halo model A0 is losing less than 20% of its initial prolateness over the first 1.5 Gyr after $z = 3$, i.e., almost three times less than the A1. It experiences almost no change in the flatness. Note, not only the mass is added in a growing disk but also angular momentum, as the new particles possess the maximal allowed J at the radii of their insertion.

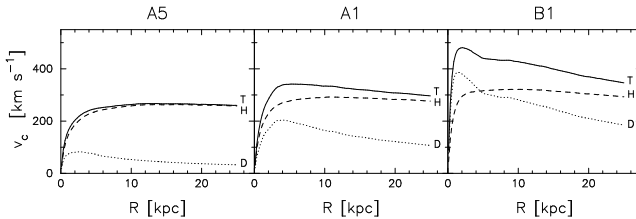


FIG. 6.— Rotation curves for A5 (time $\tau_i = 1.81$ Gyr), A1 ($\tau_f = 2.84$ Gyr) and B1 ($\tau_f = 4.87$ Gyr) models. Dashed line shows the halo contribution, dotted line — the disk contribution, and solid line — the total rotation curve.

The rotation curves for models A5, A1 and B1 shown in Fig. 6 correspond to the time when the disk reaches its maximal mass. The dynamical importance of the disk grows along this sequence — while A5 is halo-dominated at all radii, B1 hosts a *maximal* disk, in the sense of dominating the mass of the inner region. We note that the halo mass is dragged inward in our models because the disks are inserted nearly adiabatically and initially have a negligible mass compared to that of the halo within the same radius. This increase in the halo's central mass concentration is an artifact, because of the lack of clumpy baryons in our simulations, and leads to an overall increase in the halo cuspiness.

3.3. Evolution with the growing seed disk — model A1

In the *initial* response of the seed disk to the triaxial halo, a bar-like structure forms immediately and fully dissolves ~ 1 Gyr later. At the dissolution time, the disk has already reached its full mass. The halo triaxiality gets reduced significantly, compared to the pure DM model A0, and the halo becomes essentially axisymmetric. Because the disk insertion is quasi-adiabatic, the DM cusp is not destroyed but becomes even somewhat more pronounced, which is purely an artifact of our way of introducing the disk (see Section 3.2.1).

Following the dissolution of the original response to the prolate halo, the disk stays slightly oval for a prolonged period of time, in excess of ~ 1 Gyr. For brevity, we define the disk as being barred when the amplitude of $m = 2$ mode $A_2 \gtrsim 0.1$, in all models. Using this convention, the bar in A1 reappears at ~ 4 Gyr, this time as a result of a dynamical bar instability. The details of the bar growth and evolution are shown in Fig. 7 and the Animation Sequence 2 — the bar experiences the vertical buckling instability at $\tau \sim 5.9$ Gyr, weakens and continues to grow secularly, in strength and size, for another 2 – 2.5 Gyr thereafter, when it saturates. The pattern speed of the $m = 2$ disturbance in the disk is very low initially, but when the bar reappears, it is $\sim 50 \text{ km kpc}^{-1} \text{ s}^{-1}$. This change can be explained by the small initial central mass concentration in the model. On the other hand, the fully grown disk adds substantially to the central mass and, in addition, drags some of the DM inward due to the adiabatic way of insertion.

The bar in A1 reaches its full strength and size only after the vertical buckling, $z \sim 0.5$, but the full disk is in place by $z \sim 2$. What is the reason for this delay of ~ 4 Gyr, which is comparable to ~ 10 disk rotations within the bar-unstable region of 10 kpc? Typically, the strong bar appears after 2–3 disk rotations, e.g., as in the axisymmetric models LS1–3 of Berentzen et al. (2006), if N is sufficiently large and the discreteness noise is relatively low. We return to this issue in Section 4.

The initial halo prolateness triggers a response in the disk, with an amplitude, A_2 , comparable to the halo's $m = 2$ amplitude, i.e., to the degree of its prolateness. This response in the disk has a position angle which is normal to that of the halo major axis and basically represents an oval distortion in the inner disk. Both modes,

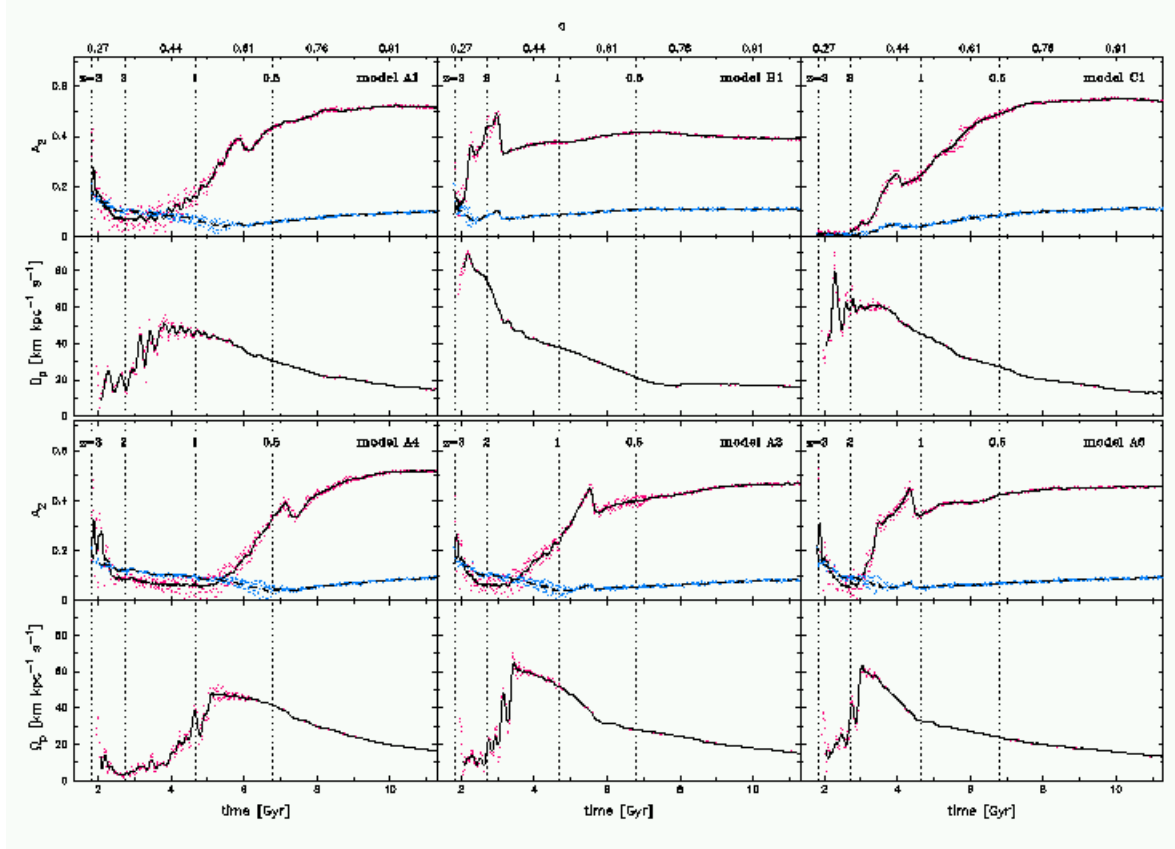


FIG. 7.— Models with growing disks that develop stellar bars. Upper panels: Evolution of stellar bars (black line) and DM halo (ghost) bars (dashed cyan line) $m = 2$ Fourier amplitudes, A_2 , integrated within the central 5 kpc. Lower panels: Bar pattern speeds Ω_b . The vertical dotted lines mark redshifts $z=3$ to $z=1$, respectively. The overall evolution of the disk-halo system for the benchmark model A1 is shown in the Animation Sequence 2, where projections on the individual planes are displayed.

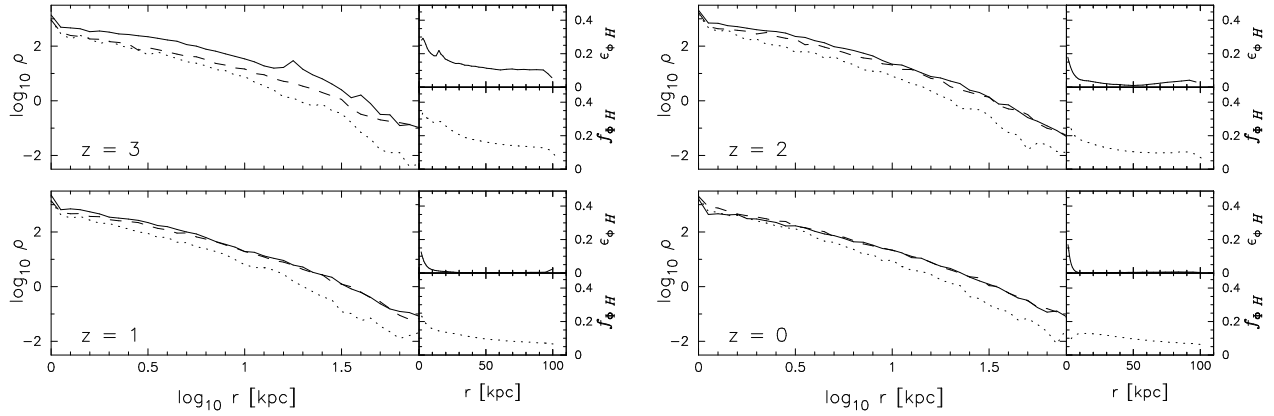


FIG. 8.— The DM halo in the model A 1. The figure shows the volume density, in units of $10^6 M_\odot \text{ kpc}^{-3}$, along the halo principal axes (left panel). The right panels show the halo prolateness (upper panel) and its flatness (lower panel). The four frames are taken at different redshifts, $z = 3, 2, 1$ and 0.

in the disk and the halo, are stagnant, because the halo's spin is negligible, and fade away with time. Also, we detect a long-lived spiral structure in the outer disk, in this and other prolate models, which was also noted by Berentzen et al. (2006). The existence of this spirals in a purely collisionless disk within a prolate halo is in a sharp contrast with the disk evolution in axisymmetric models.

As the disk becomes bar unstable, we observe that this bar always excites a 'ghost' bar in the DM halo (e.g., Athanassoula 2005). This ghost bar is a gravitational wake in the halo and not a self-gravitating entity like an actual stellar bar. Its shape differs from that of the stellar bar – it is much shorter and 'fatter' in all axial ratios. The ghost bar would dissolve abruptly if the stellar bar would disappear. It co-rotates with the stellar

bar and has the same pattern speed and nearly the same position angle. Aftermath the buckling instability (i.e., ~ 5.9 Gyr), the stellar bar continues its secular growth, and the amplitude of the ghost bar increases as well, although it always remains well below that of the disk bar.

We have used the Berentzen et al. (2006) method of isodensity fitting to estimate the bar size. In A1, it is roughly tracking the bar amplitude by dropping from the initial 5 kpc (bar semi-major axis) to ~ 3 kpc a 1 Gyr later, then increasing monotonically to about 6.5 kpc, before the secondary buckling (Martinez-Valpuesta, Shlosman & Heller 2006), and leveling off.

3.4. Evolution with a growing massive disk — model B1

We start with a three times more massive seed disk than in A1 (see Table 1). We observed some noticeable differences both in the disk and the DM halo evolution as a result. The halo prolateness within the central 20 kpc drops to near non-existent (see Fig. 5). The initial disk response to the halo is very limited in time — the onset of the dynamical bar instability cuts it off (Fig. 7). The bar which appears during the disk growth strengthens substantially in less than 0.5 Gyr, then decays slightly in order to resume its growth for another 1 Gyr. It buckles vertically at ~ 3 Gyr, which reduces its strength dramatically. The bar resumes its secular growth thereafter. For redshifts $z < 0.5$, the bar amplitude A_2 within the central 5 kpc shows a slight (but monotonic!) sign of decrease.

The A_2 amplitude (i.e., prolateness) in the halo decays initially. The halo ghost bar develops alongside the stellar bar, experiences a sharp drop in the amplitude during the stellar bar buckling, and resumes its secular growth subsequently.

The evolution of the pattern speed of the disk bar differs in this model from that of A1 as well. The stellar bar appears tumbling dramatically faster at $\Omega_b \sim 90$ km kpc $^{-1}$ s $^{-1}$. It decays strongly over the evolution time of this model. This behavior characterizes an efficient J -transfer from the disk to the DM halo over the first 6 Gyr of the bar life and a nearly complete absence of such an interaction in the next 3 Gyr.

Furthermore, the bar size follows its A_2 variation on the average. The bar grows rapidly to above 7 kpc at $\tau \sim 2.3$ Gyr, then drops to ~ 5 kpc over the next Gyr. Interestingly, this drop corresponds to the sudden change in the bar growth (see above) and is clearly visible in Fig. 7. For the rest of the evolution, the bar size stabilizes and decays very slowly in the 8–9 kpc range. All three major characteristics of the bar, namely its tumbling rate, bar strength and size, correlate — all remain nearly constant over a prolonged period of time.

3.5. Evolution with growing disk in axisymmetric halo — model C1

For a comparison, we have repeated the A1 model evolution in an axisymmetric halo. To create this halo, we take a ‘snapshot’ of A0 at $z=3$ and redistribute the particles azimuthally in the random fashion. We kept the original planar radius of particles unchanged and maintained the halo flattening. Afterwards we have truncated the halo at 75 kpc. We have added the disk to the model and relaxed it for $\Delta\tau=50$. Finally, we have assigned velocities in the disk based on the new axisymmetric halo particle distribution.

Naturally, the seed disk-halo system is in dynamical equilibrium at the time of insertion, hence no initial disk response to the halo is expected (and observed). The bar starts to grow in ~ 1 Gyr and buckles subsequently, then resumes its growth which saturates secularly (Fig. 7). The ghost bar behaves similarly and weakens during the stellar bar buckling, with the follow up growth.

The stellar bar size grows substantially over the period of ~ 2 Gyr. At the buckling time, the bar size stabilizes around 6 kpc and then experiences a very shallow secular increase to ~ 7.5 kpc, dropping 0.5 kpc at the end of the evolution.

3.6. Evolution with slowly growing disk — model A4

In this model we grow the disk over 3 Gyr after its insertion. The initial response in the disk is the same as in A1 and so is the final structure of all components (disk, bar and the halo). The halo triaxial shape is similar as well, with its prolateness remaining slightly larger than in A1 (Fig. 5). The (initial) halo prolateness is correspondingly more long-lived. The main difference between A4 and A1 is that the stellar bar starts to form ~ 2 Gyr later (Fig. 7) — which is consistent with the similarly slower disk growth in this model. We relate this delay in the bar growth to a protracted addition of the angular momentum (J) to the disk, as the particles are added with the maximal J at each energy. To test this, we have run a model with lower J per added particle, model A6 below.

3.7. Evolution with a low angular momentum growing disk — model A6

In order to decrease the angular momentum of the newly added particles to the growing disk (see model A4), we have re-run the A1 by assigning only 85% of the circular velocity for the new particles. The particles have been added only along the major axis of the disk (determined from the moment of inertia) in order to provide some degree of azimuthal coherency to the growing disk. It seems that the disk in A6 is more centrally concentrated than in A1 because of the large radial excursions of newly added particles with less than maximal J .

The resulting disk evolution differs from that of A1 and A4 (Fig. 7). The stellar bar appears much earlier at ~ 3 Gyr and its nonlinear growth rate is much higher. As a result, the stellar bar buckles substantially earlier than in A1. However, asymptotically its evolution converges to that of A1, both in strength and in pattern speed. The corresponding initial halo response decays faster as well and the ghost bar strengthens in tandem with the secular growth of the stellar bar.

Hence, addition of particles on the lower angular momentum orbits triggers the bar instability with a higher growth rate, which appears to be sensitive to the relatively mild removal of J , only 15%, from the disk. In fact, in A6, the stellar bar starts to form immediately after the initial disk response has been washed out (Fig. 7) — about 1 Gyr earlier than in model A1. This confirms our previous suggestion that our method of adding mass to the disk, i.e., with maximal angular momentum at each radius acts as to delay the bar instability. To test this, we have run the C6 model, which differs from A6 only by having an axisymmetric halo. We shall return to this issue in Section 4.

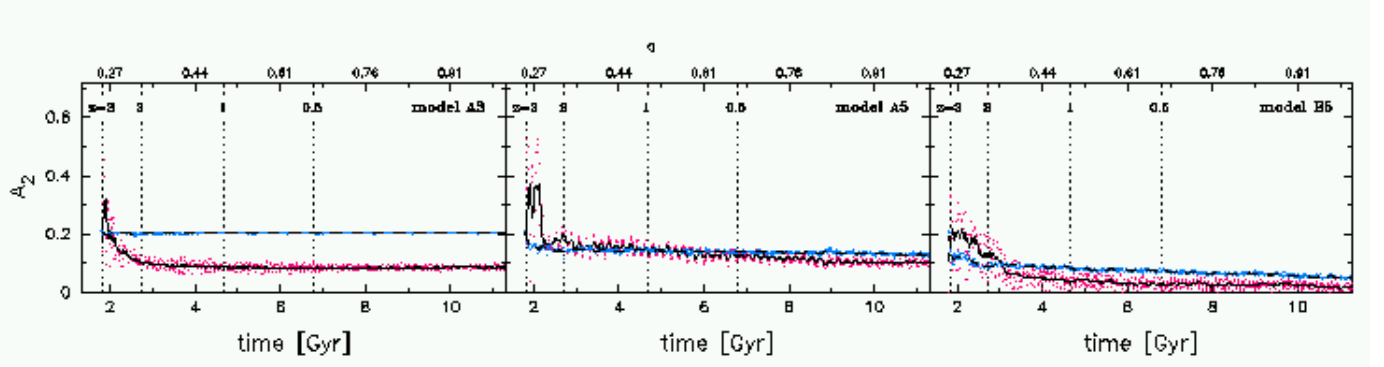


FIG. 9.— Same as the upper frames of Fig. 7, but for the models with ‘failed’ stellar bars.

3.8. Evolution with growing thin disk — model A2

Instead of giving the newly added particles *vertical* positions based on the Miyamoto-Nagai distribution function, we have assigned their positions randomly, between $z = \pm 100$ pc. This was done in order to make the growing disk colder and thus more susceptible to the bar instability. Fig. 7 shows that the stellar bar appears somewhat earlier, grows faster, but asymptotically is weaker than in A1. The halo shape is nearly identical to that of A1.

3.9. Evolution with growing disk in a frozen triaxial halo — model A3

This model was run in order to test the disk response to the undiluted prolateness of the rigid halo potential. The disk shows a strong initial response which decays abruptly to some residual amplitude which is maintained by the halo prolateness. The disk grows as in A1 but no stellar bar appears over the Hubble time of its evolution (Fig. 9). There can be a dual reason for this: either the mass of the disk is so small that the outer disk cannot absorb enough of the angular momentum of the inner few kpc, or the actual bar instability is damped by the substantially triaxial halo, as argued by El-Zant & Shlosman (2002) and Berentzen et al. (2006). We have ruled out the former possibility by evolving the same disk in a frozen axisymmetric halo — a strong bar has appeared in this case. Hence this model confirms both the theoretical predictions and the previous live numerical simulations that the bar instability is strongly damped by the halo prolateness, especially in frozen halos which lack the ability to adjust and to wash out their asymmetry.

3.10. Evolution with a non-growing disk — model A5

We start with the default disk, as in the A1 model, but the seed disk does not grow. As in A1, a bar-like feature forms due to the initial response to the triaxial halo and dissolves linearly with time. The residual A_2 amplitude both in the disk and in the DM halo have the same value (Fig. 9) and can be simply explained as driven by the halo prolateness. Because the mass of the disk remains small compared to the halo mass within the same radius, the disk has no visible effect on the halo shape evolution, except that its insertion reduced the halo triaxiality somewhat, compared to the pure halo

model A0. But this effect is substantially smaller than for the growing disk in A1. The model A5, in fact, tests to what degree the seed disk affects the halo evolution.

3.11. Evolution with a more massive non-growing disk — model B5

One can suggest, based on the evolution of the B1, that the main reason for the difference in the bar growth is the initially more massive seed disk. However this is contradicted by the B5 model, where we use the same massive seed disk but keep its mass constant. Overall impression of B5 is that it closely resembles the A5 model (Fig. 9). This test model, therefore, provides a strong argument that it is not the initial mass of the disk which is important but rather its final mass.

3.12. Bar sizes, disk radial scalelengths and central bulges

In all of the models, bars appear to evolve only in axisymmetric halos or halos which lost their prolateness during the disk growth. The timescale of the disk growth has no effect on the resulting bar size: models A1 and A4 develop nearly identical bars with semimajor axis of $r_b \sim 8$ kpc and a very similar history. Axisymmetric disk in C1 leads to the same bar as in A1, and so is the massive disk in B1. The low angular momentum disk in A6 results in a somewhat smaller bar of $r_b \sim 5 - 6$ kpc. This can be explained by a more centrally concentrated disk here. Overall, the bar maximal size appears to be close to the DM cusp size $R_s \sim 7$ kpc in A0.

The disk growth in our models leads to the increase in the central density. We find, however, that models that host stellar bars develop much larger central densities after the period of the bar instability. More massive disks growing adiabatically drag in the DM which results in substantially higher central densities, especially in B1. Therefore, unlike in Berentzen et al. (2006), we find that the surface density in the current disks can be approximated by a single-exponential law plus a central ‘bulge,’ instead of a double-exponential law. This ‘bulge’ region corresponds to the axisymmetrized stellar bar part of the disk, and we refer here to the bulge only in the context of a density fitting.

The surface density in the outer disk, beyond the bar, was fit with an exponential profile, $\Sigma(r) =$

$\Sigma_o \exp(-r/r_d)$, where Σ_o is the normalization constant and r_d is the disk exponential scalelength. The resulting exponential law has been extrapolated to the center and the excess surface density was considered as a bulge contribution. The bulge surface density then has been fit by the profile $\Sigma(r) = \Sigma_i \exp[-(r/r_{bg})^{1/n}]$, where n —the shape parameter corresponds to the pure exponential ($n = 1$) or de Vaucouleurs ($n = 4$) profiles, r_{bg} is bulge's radial scalelength and Σ_i its central density (Sérsic 1968; Binney & Merrifield 1998). For A1, we find that $n \approx 0.8$ during the entire simulation, and $r_{bg} \sim 2.3$ kpc when the full disk is in place. The scalelength r_{bg} increases somewhat to 2.7 kpc until the bar buckles at 5.9 Gyr and then decreases secularly towards 2 kpc, due to the action of the bar which becomes more centrally concentrated after the buckling instability. The ratio r_b/r_{bg} changes, therefore, from ~ 1.9 at the buckling to ~ 4 at the end of the simulation. The exponential scalelength of the outer disk stays around 3.3 kpc after the disk stops growing.

3.13. Disk tumbling

All disk models in our simulations have been permitted to move freely in response to the streamers in the assembling halo and interactions with halo substructure. We have detected that the disk plane in model A1 starts to tilt very slowly around an axis in its plane about 2 Gyr after the disk insertion (e.g., Animation Sequence 2) and so in other models as well. This motion has a counterpart in the inner halo, within ~ 50 kpc and the equatorial planes of the disk and the halo remain aligned over all the length of the simulation. The reason for this motion in the halo lies in the streamers excited by the halo substructure. As a result, we typically do not detect a warping of the disk midplane, except for some short periods of time. The disk also does not precess for the same reason.

3.14. Velocity anisotropy in the DM halo

Hansen & Stadel (2006) have claimed a correlation between the density slope of the DM halo, $\alpha \equiv d\ln\rho/d\ln r$, and the anisotropy parameter, $\beta = 1 - \sigma_t^2/\sigma_r^2$, where σ_t and σ_r are tangential and radial velocity dispersions in the DM. Specifically, they propose a correlation $\beta = -0.2(\alpha + 0.8)$ over about three orders of magnitude in r within the DM cusp, with an intrinsic scatter in β of 0.05, for slopes with $\alpha > -3$. We have measured both α and β for two of our models, pure DM model A0 and our benchmark model A1. Our best fit for A0 halo is $\beta = -0.17(\alpha - 1.68)$ for a comparable range in r (Fig. 10). The halo in A1 fits the same relation as in A0. Hence, we confirm the slope in the correlation proposed by Hansen & Stadel, but find the curve being significantly offset from their value.

4. DISCUSSION

We have investigated the evolution of growing stellar disks within assembling asymmetric DM halos, by means of high-resolution N -body simulations. The halos have been constructed using constrained realizations in the linear regime and evolved from cosmological initial conditions. We have inserted the ‘seed’ disks at the center of mass of the innermost halo, at the redshift $z = 3$, after the end of the violent (merger) phase in the halo evolution. The seed disks, with 10% of their final mass, have

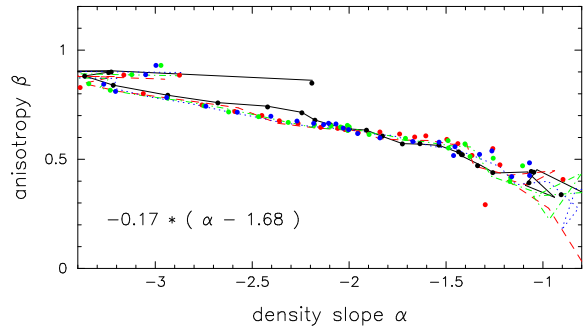


FIG. 10.— Inner dispersion velocity anisotropy parameter β vs. density slope parameter $\alpha \equiv d\ln\rho/d\ln r$ for the DM halos in models A0 (lines) and A1 (dots) at different times. The color coding is as follows: black at 1.81 Gyr, red at 2.84 Gyr, green at 7.09 Gyr and blue at 11.3 Gyr.

been grown over a period of 1–3 Gyr thereafter. These disks have been allowed to move freely within the halo in response to the interactions with the inner and outer substructure and with the streamers within the halo. For comparison, we have run additional models with more massive disks, non-growing disks, frozen disks, or disks in frozen halos, etc.

Our main result is that a growing disk is responsible for washing out the halo prolateness and, to a lesser degree, the halo flatness, over a period of time comparable to its growth. We find that *massive* disks which contribute more to the overall rotation curve in the system are more efficient in removing the prolateness in the halo. The halo figure rotation remains negligible during this process.

In a number of models displayed in Fig. 5, we show that the halo shape is very sensitive to the final disk mass, while being reasonably independent of how the *seed* disk is introduced into the system — abruptly or quasi-adiabatically. The timescale of the subsequent growth of the disk mass has a small effect on the halo shape as well — such a halo remains slightly more triaxial (model A4). On the other hand, when the growing disk was kept frozen, the halo lost slightly more of its prolateness (model A1b). This has happened because the disk was not able to adjust its shape to that of the surrounding halo in the latter case.

The corollary is that the maximal disks most probably reside in nearly axisymmetric DM halos. On the other hand, *light* disks whose rotation remains halo-dominated at all radii have progressively smaller effect on the halo shapes and are expected to reside in somewhat diluted but prolate halos. Consequently, we envisage that massive disks are prone to development of large-scale stellar bars (unless additional adverse factors prevail), while light disks have the bar instability damped by the halo triaxiality.

These corollaries from numerical simulations are complementary and bear interesting observational and evolutionary consequences for disk galaxies embedded in DM halos. Previous theoretical study (El-Zant & Shlosman 2002) and numerical simulations (Berentzen et al. 2006) have argued that stellar bars and triaxial halos are incompatible, by-passing the issue of how such systems can form in the first place. Dubinski (1994) has shown that growing an *analytical* spherical potential inside a triaxial

halos will reduce the halo asymmetry but residual triaxiality will remain. Kazantzidis et al. (2004) have used cosmological simulations of the DM and baryonic matter to show that cooling within the halos leads to more spherical halos than in adiabatic simulations. Models presented here resolve the issue of bar-asymmetric halo incompatibility by showing explicitly that the growing disk is primarily responsible for erasing the halo prolateness and diluting its flatness, and that long-lived bars emerge only in models which become nearly axisymmetric.

Substantial differences in the subsequent evolution of disk models can be detected, depending on their growth history. This is clearly reflected in the growth rate of the bar instability. The bar formation is considerably delayed in A1 and proceeds slower in C1 compared to lower angular momentum disks in A6 (Fig. 7) and C6. The former disks have grown by a particle addition to the circular orbits, i.e., with the maximal angular momentum J for the particle orbital energy. As the bar growth is associated with the loss of J from the unstable region, the addition of J should in principle stabilize the disk, temporarily. This, however, does not explain why is it that the bar instability is postponed by a number of disk rotations after we stop adding mass to the disk in A1 but appears shortly thereafter in A6. If this difference arises solely from the additional 15% of J in A1, one should observe the same delay in model C1. However, a substantially smaller delay appears in the (axisymmetric halo) C1.

We note that the original halo prolateness is preserved for a longer period of time in A1 than in A6, as the direct comparison of halo's $m = 2$ amplitudes in Fig. 7 shows. One observes in this Figure that the stellar bar starts to grow when the halo's A_2 amplitude drops below 0.1, i.e., small $\epsilon_{\phi H}$ — in tandem with calculations based on the Liapunov exponents and in self-consistent N -body simulations of disk evolution in live triaxial halos (El-Zant & Shlosman 2002; Berentzen et al. 2006).

We have run a test model (C6) with an axisymmetric halo, as C1, but where particles have been added with 85% of J for the circular orbits — similarly to A6. Its stellar bar appears immediately after the disk has reached its final mass, by $z \sim 2$. What is evident is that, in both A6 and C6 models, the stellar bar pattern speed has a maximum which is clearly larger than in A1 and C1. The simple explanation of this is that models with lower J , A6 and C6, are more centrally concentrated than the latter models and their central dynamical timescale is accordingly shorter. Hence, at least in the linear stage, the growth rate of the dynamical instability is larger in A6 and C6. It appears that a combination of an addition of J and different central concentration govern the bar/disk evolution in the models described above.

All models developing stellar bars also develop *ghost* bars in the halo that are nearly aligned with the disk bars. Interaction between these bars is a major contributor to the slowdown of the stellar bar. The ghost bar acts as a gravitational wake and its orbital structure is fundamentally different from that of the stellar bar — in particular, the DM particles are *not* trapped within the ghost bar as they are within the stellar bar. Ghost bars are sensitive enough to respond to the vertical buckling in the stellar bars and they grow in tandem with the

stellar bars, as seen in Fig. 7. However, they should not be confused with the original halo prolateness which also contributes to the $m = 2$ amplitude, A_2 , in the halo for the first few Gyrs. We find that this latter contribution serves as a reliable indicator for the growth/decay of the stellar bars — those grow when halo's A_2 amplitude drops below 0.1.

The density profile in the disk can be fit by a single-exponential profile plus a central bulge which is somewhat steeper than an exponential. This differs from double-exponential disks that have developed in Berentzen et al. (2006) models. The reason for this difference appears to be the quasi-adiabatic insertion of the disk in the current work. This quiescent way of insertion drags in the DM, without destroying the central cusp. Berentzen et al. (1998) has found a similar bulge shape for pure collisionless models, which has been modified with the addition of the gas component in the disk. Overall we find that disk-to-bulge scalelength ratio stays in the range of 1.2 – 1.6, while bar size-to-bulge scalelength ratio increases from about 1.9 to 4. In all models, the bar has been roughly confined to within the NFW scalelength R_s .

We find that the DM halo cusps are preserved in our numerical simulations, although the quality of the NFW fit is significantly degraded with the growth of the disks. The reason for this apparent robustness of the cusps lies in the quasi-adiabatic insertion of our seed disks which, in fact, reinforce the cusps by dragging in the DM. Even in models with strong stellar bars, the cusps survive. It is possible that in reality they are destroyed by the accreting clumpy baryons (e.g., El-Zant et al. 2001, 2004) or by other similar processes (e.g., Tonini, Lapi & Salucci 2006) prior to the disk formation. This issue is beyond the scope of this work. We also did not address the possible effect that the halo cuspiness has on the halo's triaxiality (e.g., Berentzen et al. 2006).

How does the evolution of disk-halo systems described in this work fit within the broader issue of disk galaxy evolution within the cosmological context? While numerical simulations have shown that halos form as prolate and flattened entities (e.g., Bullock 2002), they appear as nearly axisymmetric (oblate) in the local universe (e.g., Merrifield 2002). On the other hand, the high frequency of stellar bars in the local and intermediate redshift universe (Jogee et al. 2004; Elmegreen et al. 2004; Sheth et al. 2003) poses a potential problem because bars and prolate halos are incompatible (El-Zant & Shlosman 2002; Berentzen et al. 2006). A process which washes out the halo prolateness, therefore, can be, in principle, responsible for the present high fraction of barred disks. For this to happen, the reduction of a halo triaxiality should be achieved *quasi-adiabatically*. Otherwise, a galactic disk will be heated up and stabilized against the bar formation for a prolonged period of time. Major mergers and even frequent minor mergers can lead to such an 'over-heating' of stellar disks. Furthermore, the major mergers will typically destroy the disks.

A gradual buildup of a galactic disk within an initially *asymmetric* DM halo can play the role of the required quasi-adiabatic process which resolves both issues at once, i.e., the halo prolateness and the high observed bar fraction. Jogee et al. (2004) have argued in favor of such a quiescent disk evolution over the last 8 Gyrs,

based on the inferred optical fraction of bars and on the distribution of bar ellipticities and sizes over $z \sim 0.2 - 1$ in recent GEMS survey with the *HST*. Moreover, Barden et al. (2005) have shown that the disk mass grows faster with redshift than its surface density. This requires a gradual increase in the disk radial scalelength with z — a method implemented here to grow the seed disks.

The scenario that emerges from this *gradual* buildup of disks within the triaxial DM halos, in principle, can explain the current population of stellar bars in disk galaxies. Within this hierarchical merging framework, the DM halos of arbitrary shapes form first during the major merger epoch. If disks form during this early stage, they are probably destroyed shortly thereafter. Disks that grow during the next quiescent epoch can be responsible for the washing out of the halo prolateness and, to a lesser degree, its flatness. The efficiency of this process depends on the increasing disk-to-halo mass ratio. Large-scale stellar bars will form under these conditions with a delay — first bars would form in systems with more massive disks and, therefore, more oblate halos. For lower redshifts, progressively more disk galaxies will be susceptible to an intrinsic (spontaneous) bar instability as contrasted by the tidally-induced bars.

Hence, bars which are observed in the local universe can still be the first generation which formed spontaneously after the host halo prolateness has been washed out. Within this scenario, the intrinsic bar formation is spread out in time. Thus, the observed fraction of stellar bars, and distributions of their strength and sizes reflects a steady state between the newly forming bars in more

axisymmetric halos and bars destroyed by various processes. The details of the above formation and destruction processes are still sufficiently unclear. For example, we do not know what is the characteristic timescale of a disk buildup. This work explores the range of 1–3 Gyrs, but, in principle, it can be much longer, $\sim 8 - 10$ Gyrs, as hinted by the results from GEMS, and, therefore, can extend beyond $z \sim 2$.

To summarize, we have developed a method to insert seed disks and to grow them subsequently in cosmologically evolving halos in a quasi-adiabatical way. We have investigated the response of the halo shape to the growing stellar disk and the feedback of the halo onto the subsequent evolution of this disk. We find that the growing disk dilutes the halo triaxiality depending on the final disk mass. Maximal disks, therefore, are expected to reside in oblate halos, while disks dominated by the halo at all radii can reside in prolate halos. Consequently, we expect that the massive disks are prone to the bar instability, while light disks have this instability damped by the halo triaxiality.

We are grateful to Yehuda Hoffman for producing the constrained realizations, to Clayton Heller for converting them into initial conditions for the DM, and to Emilio Romano-Diaz for helping with selected diagnostics in Fig. 1. This research has been partially supported by NASA/LTSA 5-13063, NASA/ATP NAG5-10823, HST/AR-10284, and by NSF/AST 02-06251 (to IS).

REFERENCES

- Abraham, R.G., Merrifield, M.R., Ellis, R.S., Tanvir, N.R., Brinchmann, J. 1999, MNRAS, 308, 569
- Athanassoula, E. 2003, MNRAS, 341, 1179
- Athanassoula, E. 2005, Nonlinear Dynamics in Astronomy and Physics (in memory of Henry E. Kandrup), eds. S.T. Gottesman, J.R. Buchler & M.E. Mahon, Ann. NY Acad. of Sci., 1045, 168
- Barnes, J., Hut, P. 1986, ApJ, 324, 446
- Barden, M. et al. 2005, ApJ, 635, 959
- Barnes, J., Efstathiou, G. 1987, ApJ, 319, 575
- Berentzen, I., Heller, C.H., Shlosman, I. 1998, MNRAS, 300, 49
- Berentzen, I., Shlosman, I., Jogee, S. 2006, ApJ, 637, 582
- Binney, J., Merrifield, M.R. 1998, Galactic Astronomy, Princeton Univ. Press
- Binney, J. Tremaine, S. 1987, Galactic Dynamics, Princeton Univ. Press
- Bullock, J.S., Dekel, A., Kolatt, T.S., Kravtsov, A.V., Klypin, A.A., Porciani, C., Primack, J.R. 2001, ApJ, 555, 240
- Bullock, J.S. 2002, The Shapes of Galaxies and Their Dark Halos, ed. P. Natarajan (Singapore: World Scientific), 109
- Dehnen, W. 2002, J. Comp. Phys., 179, 27
- Dubinski, J. 1991, ApJ, 431, 617
- Elmegreen, B.G., Elmegreen, D.M., Hirst, A.C. 2004, ApJ, 612, 191
- El-Zant, A.A., Shlosman, I., Hoffman, Y. 2001, ApJ, 560, 636
- El-Zant, A.A., Shlosman, I. 2002, ApJ, 577, 626 (ES02)
- El-Zant, A.A., Hoffman, Y., Primack, J., Combes, F., Shlosman, I. 2004, ApJ, 607, L75
- Frenk, C.S., et al. 1999, ApJ, 525, 554
- Governato, F., Willman, B., Mayer, L., Brooks, A., Stinson, G., Valenzuela, O., Wadsley, J., Quinn, T. 2006, MNRAS, submitted, astro-ph/0602351
- Halir, R., Flusser, J. 1998, Int. Conf. in Central Europe on Comp. Graphics, Visualization & Interactive Digital Media, 125
- Hansen, S.H., Stadel, J. 2006, astro-ph/0510656
- Heller, C.H., Shlosman, I. 1994, ApJ, 424, 84
- Heller, C.H. 1995, ApJ, 455, 252
- Hoffman, Y., Ribak, E. 1991, ApJ, 380, L5
- Holley-Bockelmann, K., Weinberg, M., Katz, N. 2005, MNRAS, 363, 991
- Immeli, A., Samland, M., Gerhard, O., Westera, P. 2004, A&A, 413, 547
- Jogee, S., Knapen, J.H., Laine, S., Shlosman, I., Scoville, N.Z., Englmaier, P. 2002a, ApJ, 570, L55
- Jogee, S., Shlosman, I., Laine, S., Englmaier, P., Knapen, J.H., Scoville, N.Z., Wilson, D.D. 2002b, ApJ, 575, 156
- Jogee, S., Barazza, F.D., Rix, H.-W., Shlosman, I. et al. 2004, 615, L105
- Kazantzidis, S., Kravtsov, A.V., Zentner, A.R., Allgood, B., Nagai, D., Moore, B. 2004, ApJ, 611, L73
- Martinez-Valpuesta, I., Shlosman, I., Heller, C.H. 2006, ApJ, 637, 214
- McMillan, P.J., Denhen, W. 2005, MNRAS, 363, 1205
- Merrifield, M.R. 2002, The Shapes of Galaxies and Their Halos, Ed. P. Natarajan (World Scientific), 170
- Miyamoto, M., Nagai, R. 1975, PASJ, 27, 533
- Navarro, J.F., Frenk, C.S., White, S.D.M. 1997, ApJ, 490, 493 (NFW)
- Peebles, P.J.E. 1969, ApJ, 155, 393
- Rix, H.-W. et al. 2004, ApJ Suppl., 152, 163
- Rix, H.-W., Zaritsky, D. 1995, ApJ, 447, 82
- Romano-Diaz, E., Hoffman, Y., Faltenbacher, A., Jones, D., Heller, C., Shlosman, I. 2006a, ApJ, 637, L93
- Romano-Diaz, E., Faltenbacher, A., Jones, D., Heller, C., Hoffman, Y., Shlosman, I. 2006b, ApJ, submitted
- Sellwood, J.A. 2003, ApJ, 587, 638
- Sellwood, J.A. 2006, ApJ, 637, 567
- Sérsic, J.L. 1968, Atlas de Galaxias Australes (Córdoba: Observatorio Astronómico)
- Sheth, K., Regan, M.W., Scoville, N.Z., Strubbe, L.E. 2003, ApJ, 592, L13
- Sommer-Larsen, J., Götz, M., Portinari, L. 2003, ApJ, 596, 47
- Tonini, C., Lapi, A., Salucci, P. 2006, submitted (astro-ph/0603051)
- Weinberg, M.D. 1985, MNRAS, 213, 451
- Weinberg, M.D., Katz, N. 2002, ApJ, 580, 627